Modeling of air-gap membrane distillation process: A theoretical and experimental study

A.S. Alsaadi[a], N. Ghaffour[a], J.-D. Li[b], S. Gray[c], L. Francis[a], H. Maab[a], G.L. Amy[a]

[a]Water Desalination and Reuse Center, King Abdullah University of Science and Technology (KAUST), 23955-6900 Thuwal, Saudi Arabia, Tel. +966-28082180, Email: noreddine.ghaffour@kaust.edu.sa

[b]School of Engineering and Science, Victoria University, P.O. Box 14428, Melbourne, Victoria 8001, Australia

[c]Institute of Sustainability and Innovation, Victoria University, P.O. Box 14428, Melbourne, Victoria 8001, Australia

Abstract

A one dimensional (1-D) air gap membrane distillation (AGMD) model for flat sheet type modules has been developed. This model is based on mathematical equations that describe the heat and mass transfer mechanisms of a single-stage AGMD process. It can simulate AGMD modules in both co-current and counter-current flow regimes. The theoretical model was validated using AGMD experimental data obtained under different operating conditions and parameters. The predicted water vapor flux was compared to the flux measured at five different feed water temperatures, two different feed water salinities, three different air gap widths and two MD membranes with different average pore sizes. This comparison showed that the model flux predictions are strongly correlated with the experimental data, with model predictions being within $\pm$10% of the experimentally determined values. The model was then used to study and analyze the parameters that have significant effect on scaling-up the AGMD process such as the effect of increasing the membrane length, and feed and coolant flow rates. The model was also used to analyze the maximum thermal efficiency of the AGMD process by tracing changes in water production rate and the heat input to the process along the membrane length. This was used to understand the gain in both process production and thermal efficiency for different membrane surface areas and the resultant increases in process capital and water unit cost.

Keywords: Air-gap membrane distillation (AGMD); Modeling; Thermal efficiency; Co-current and counter-current flow regimes; Scale-up.

1. Introduction

Membrane Distillation (MD) is a thermally driven separation process that utilizes a hydrophobic, micro-porous membrane as a contactor between two fluids maintained at different temperatures where the separation is achieved by the mass transfer of the vapor phase. At relatively low operating pressures the hydrophobicity of the micro-porous membrane prevents the liquid phase from wetting the membrane pores and vapor is the only phase to pass through the membrane. The difference in fluid temperatures between the two sides of the membrane creates a driving force for the vapor to pass from the fluid at higher temperature (feed) to the one at lower temperature (coolant).

MD holds high potential for several applications including water desalination [1]. It is an alternative sustainable technology that can be driven by solar, geothermal or waste heat [2]. One of the main advantages of MD is that process performance is not highly affected by high feed salinity, as was proven in bench scale [3,4] and in full scale [5] studies.

Air Gap Membrane Distillation (AGMD) is one of the four common MD configurations. It is characterised by the presence of a stagnant air gap between the membrane and the condensation surface to reduce the heat loss by conduction. Because of the improved thermal efficiency of AGMD compared to direct contact membrane distillation (DCMD), it became the first choice for pilot testing to address scale-up and long-term operational issues [5-9]. This may be due to the close similarity of the AGMD configuration to the matured Multi-Stage Flash (MSF) technology. The former technology can be described as an intensification of the latter one. In other words, even though the two technologies share many similar features, AGMD is reduced in size compared to MSF, because of its higher surface area to volume ratio, and can possibly achieve the same level of production and thermal efficiency. Furthermore, it holds future potential advantages over the conventional thermal-based processes such as:

- It can be decentralized since it is modular and any low grade heat source (solar energy, waste-heat) can be sufficient for its operation.
- AGMD modules can be made of inexpensive polymeric materials that are corrosion resistant.
- As is the case with most membrane-based separation technologies, the MD operation procedure is simple and requires relatively less manpower [10].

– Low operation and maintenance cost and no chemicals required [11].

Modeling of AGMD processes has generally taken either of two approaches: 0-dimensional modeling (0-D) where the transport of heat and mass are averaged over the module, and two-dimensional modeling (2-D) where variations in heat and mass transfer conditions along the membrane are taken into consideration (i.e., temperature profiles, hydrodynamics). The limitations of these approaches are:

- 0-D models [12-20]: these models do not consider the changes of the fluid conditions as they flow inside the AGMD module. Averaged fluids properties are used as inputs to these models. Such models do not account for changes in temperature (and therefore driving force) along the membrane length, and process scale-up can only be predicted from experiments using an AGMD module of the same dimensions and identical operating conditions (i.e., pilot plant trials). Therefore, this approach can neither be used for optimization nor can it predict performance from small scale laboratory experiments or conditions for which experiments have not been conducted.

- 2-D models [21-24]: these models involve detailed computational fluid dynamic (CFD) simulation of the flow parameters and heat transfer across a 2-dimentional membrane surface. Such models are computationally intensive and require longer time to achieve results, especially for large membrane surface areas. Given that the configuration of most AGMD systems are flat sheet membranes where the conditions are assumed to be identical across the membrane width, the extra complication of 2-D modeling compared to 1-dimentional modeling (1-D) appears unnecessary.

To the authors' knowledge, there has been only one 1-D model for AGMD reported in the literature to date, although 1-D modeling of DCMD has become established [25-28]. Guijt et al. [29] developed a 1-D model for a single hollow fiber module using the Dusty gas model and considered counter-current flow only. In this paper, a 1-D AGMD model for a flat sheet module was developed for both co-current and counter-current flow regimes. The theoretical model predictions were validated and compared with experimental results obtained using a locally designed and fabricated AGMD module and commercially available PTFE membranes of two different pore sizes.

2. Model development

The 1-D AGMD mathematical model developed was for flat sheet membranes typically used in commercial MD pilot units. The model is based on dividing the AGMD module longitudinally into small elements. Within each element, different zones exist where significant mass and energy exchange occurs along the boundaries of these zones. As depicted in Figure 1, the zones, in order from left to right, are as follows:

- The hot fluid channel
- The polymeric membrane layer
- The air gap space
- The condensate film on the cooling plate
- The cooling plate sheet
- The cold fluid channel

Figure 1: A schematic diagram of AGMD longitudinal zones used in describing the model.

In Figure 1, it is assumed that flow direction, x, is the same as that of the hot feed flow, and each small element is assumed to have a length of dx and a constant width W. Moreover, the mathematical model calculations were simplified according to the following assumptions:

1. The system is at steady state condition.
2. The hot and cold fluids are assumed to flow in the *x* direction only.
3. The pressure inside the air gap is constant (no pressure drop along the air gap zone).
4. The condensation on the cooling plate is film-wise and the thickness of the falling film inside the air gap is small in comparison with the width of the air gap.
5. Within the air gap, there is no bulk velocity of the air-vapor mixture. Heat is transferred by conduction while mass is transferred through diffusion.
6. Pure water vapor is only transported through membrane pores.
7. There is no heat being exchanged with the surrounding.

A magnification of two consecutive slices to illustrate the exchange of mass and heat is shown in Figure 2.

Figure 2: Magnification of two consecutive slices along an AGMD module.

The mass and energy balances of slice i in the hot fluid channel can be described as follows:

$$\Delta m_{hi} = m_{hb}{}^i - m_{hb}{}^{i-1} \tag{1}$$

$$m_{hb}{}^i S^i = m_{hb}{}^{i-1} S^{i-1} \tag{2}$$

$$Q_h{}^i dx^i W = m_{hb}{}^i c_{p_{hb}}{}^i T_{hb}{}^i - m_{hb}{}^{i-1} c_{p_{hb}}{}^{i-1} T_{hb}{}^{i-1} \tag{3}$$

where $\Delta m_h{}^i$ is the change in the hot feed mass flow rate of slice i, $m_{hb}{}^i$, S^i, $m_{hb}{}^{i-1}$ and S^{i-1} are the hot feed mass flow rates and salt mass fractions exiting and entering slice i, respectively, $Q_h{}^i$ is the hot feed heat flux of slices i, $c_{phb}{}^i$, $T_{hb}{}^i$, $c_{phb}{}^{i-1}$ and $T_{hb}{}^{i-1}$ are the specific heat and bulk temperature of the hot feed exiting and entering slice i, respectively.

The boundary layer was assumed to be a fully developed and transfers the mass that it receives from the hot fluid channel slice through convection to the membrane layer as compensation for the mass lost through evaporation.

$$\Delta m_{hb}{}^i = J_v{}^i dx^i W \tag{4}$$

where $J_v{}^i$ is the mass flux of the water vapor and W is the width of the flat sheet module. Heat is also transferred by conduction in this slice from the hot fluid channel to the membrane layer according to the following equation:

$$\Delta Q_{hi} = H_h{}^i (T_{hb}{}^i - T_{hm}{}^i) \tag{5}$$

The heat transfer coefficient $H_h{}^i$ can be calculated from the following correlation:

$$H_{hi} = \frac{Nu k_l}{d_h} \tag{6}$$

where Nu is Nusselt's number, k_l is the hot fluid thermal conductivity and d_h is the hydraulic diameter of the hot channel. For a spacer filled channel, although the Reynolds number (Re) is generally less than 300, Zhang et al. [28] suggest that model predictions fit experimental data more accurately when the streams are assumed to be fully developed turbulent flow for the calculation of Nu. Thus, Nu can be calculated from the following correlation after correcting for the spacer effect by K_s.

$$Nu = 0.029 K_s Re^{0.8} Pr^{0.33} \tag{7}$$

$$K_s = 1.904 \left(\frac{d_f}{h_s}\right)^{-0.039} \varepsilon_s{}^{0.75} \sin\left(\frac{\theta}{2}\right)^{0.086} \tag{8}$$

Where Pr is Prandtl number, d_f is the spacer filament diameter, h_s is the spacer thickness, ε_s is the spacer porosity and θ is the angle that filaments make when they cross each other.

The spacer porosity can be calculated as follow:

$$\varepsilon_s = 1 - \frac{V_{filament}}{V_{total}}$$

(9)

where $V_{filament}$ and V_{total} are the volume of the filament and the whole spacer, respectively.

The local Re number in equation (7) can be computed from:

$$\mathbf{Re} = \frac{\rho d_h V}{\mu}$$

(10)

where ρ, V, μ are the density, velocity and viscosity of the hot fluid in spacer-filled channel, respectively, and d_h is the hydraulic diameter of a spacer filled channel. The hydraulic diameter for a single sized filament of rhombus mesh spacer can be calculated by [30]:

$$d_h = \frac{4.0 \varepsilon_s d_f h_s}{2 d_f + 4(1 - \varepsilon_s) h_s}$$

(11)

The same calculations are applied for the heat transfer coefficient of the flow in the cold channel. Furthermore, at steady state, the change in heat flux of the hot feed (Q^i_h) and the change in heat flux of the coolant (Q^i_c) are equal and can be referred to as simply Q^i. However, the mass flow rate of the coolant is constant but that of the hot feed decreases because it loses water vapor through the membrane (permeate) as it flows down the module. The following equation can be used to quantify the amount of vapor that passes through the membrane pores:

$$J_v = C(P'_{hm} - P'_{ma})$$

(12)

where C is the membrane mass transfer coefficient, P'_{hm} is the saturation pressure of water at T_{hm}, P'_{ma} is the partial pressure of water vapor at the interface between the membrane and the air gap.

In calculating the mass transfer coefficient, Zhang et al. [28] concluded that, for DCMD, the Knudsen-molecular diffusion is the dominating mass transfer mechanism within the pores of the membrane and the vapor flux can be calculated as:

$$\frac{1}{J_v} = \frac{1}{J_{mv}} + \frac{1}{J_{kv}} \qquad (13)$$

where J_{mv} and J_{kv} are the vapor fluxes due to molecular diffusion and Knudsen diffusion, respectively. In other words, the total membrane resistance to water vapor can be written as a combination of two mass transfer resistances in series according to the following equation:

$$R_v = R_{mv} + R_{kv} \qquad (14)$$

where R_{mv} is the mass transfer resistance exerted by all non-condensable gases within the membrane pores on the water vapor molecules, and R_{kv} is the mass transfer resistance due to the momentum loss during the collision of water vapor molecule with the internal walls of the membrane pores. When there are no non-condensable gases within the membrane pores the resistance of R_{mv} becomes nil and the water vapor mass flux is mainly controlled by Knudsen diffusion mechanism. At high partial pressure of non-condensable gases within the membrane pores, the mass transfer is mainly controlled by molecular diffusion mechanism. The Knudsen and molecular diffusions can be calculated through the following equations [28]:

$$J_{kv} = \frac{4}{3}\frac{d\varepsilon}{b\tau}\sqrt{\frac{M_v}{2\pi RT}}(P'_{hm}-P'_{ma})$$
$$J_{mv} = \frac{M_v}{1-y}\frac{\varepsilon D_{AB}}{\tau bRT}(P'_{hm}-P'_{ma}) \qquad (15)$$

where d, b, τ, ε are the average diameter of pores, the membrane thickness, the tortuosity of the pores and the porosity of the membrane, respectively. M_v is the molecular weight of water, R is the universal gas constant, and y is the mole fraction of water vapor in the membrane pores.

The mass diffusivity between the air and water vapor is given by [31]:

$$D_{AB} = \frac{1.895 \times 10^{-5} T^{2.072}}{P} \qquad (16)$$

where T is the average temperature and P is the total pressure. The mole fraction of water vapor is related to vapor pressure P_v as:

$$y = \frac{P_v}{P} \qquad (17)$$

Combining equations 13, and 15-17 yields:

$$J_v = \frac{7.81 d\varepsilon}{b\tau}\frac{M_v T^{1.072}}{5.685\sqrt{2\pi RM_v T} + 4dR(P-P_v)}(P'_{hm}-P'_{ma}) \qquad (18)$$

Therefore,

$$C = \frac{7.81 d\varepsilon}{b.\tau} \frac{M_v T^{1.072}}{5.685\sqrt{2\pi R M_v T} + 4dR(P - P_v)} \tag{19}$$

The total heat flux across the membrane can be calculated as:

$$Q^i = \frac{k}{b}(T_{hm}{}^i - T_{ma}{}^i) + J_v{}^i h_g \tag{20}$$

where h_g is the enthalpy of the water vapor. The average thermal conductivity of the membrane is calculated by:

$$k = \varepsilon k_{air} + (1 - \varepsilon)k_m \tag{21}$$

where k_{air} and k_m are the thermal conductivities of the air and the membrane material, respectively. In equation (20), the first term is the sensible heat transfer through conduction and the second term is the latent heat transfer of water.

For a small mole fraction of water vapor within the air gap channel, the mass transfer of the water vapor can be approximately determined by [32]:

$$\bar{J}_v{}^i = \frac{cD_{AB}{}^i}{\delta_a}(y_{ma}{}^i - y_f{}^i) \tag{22}$$

where $\bar{J}_v{}^i$ is the molar flux of water vapor and is related to $J_v{}^i$ by the molar mass of water vapor, c is the total molar concentration, δ_a is the air gap width, $D_{AB}{}^i$ is the diffusivity coefficient, $y_{ma}{}^i$ is the mole fraction of water vapor at $T_{ma}{}^i$ and $y_f{}^i$ is the mole fraction of water vapor at the interface of the falling film and is a function of the saturation pressure of the water at T_f^i.

The heat transfer within the air gap can be calculated by:

$$Q^i = \frac{k_{AB}{}^i}{\delta_a}(T_{ma}{}^i - T_f{}^i) + \bar{J}_v{}^i \bar{h}_g{}^i \tag{23}$$

where $k_{AB}{}^i$ is the thermal conductivity of the gas mixture of air and water vapor and $\bar{h}_g{}^i$ is the molar enthalpy of water vapor.

For the falling film, the model of Nusselt film condensation on a vertical plate is used [33]. The condensate film thickness in that model is determined by:

$$\frac{dm^i}{dx^i} = \frac{\rho_l{}^i(\rho_l{}^i - \rho_{av}{}^i)g(\delta_f{}^i)^2}{\mu^i}\frac{d\delta_f{}^i}{dx^i} = J_v{}^i \tag{24}$$

where dm^i / dx^i is the rate of mass increase of the falling film in slice i and this should be equal to the mass transfer of the water vapor J_v^i, ρ_l^i is the density of water liquid, ρ_{av}^i is the density of the gas mixture, δ_f is the thickness of the falling film, g is the gravity acceleration, and μ_l^i is the dynamic viscosity of the water liquid.

The heat transfer across the falling film is simply computed from:

$$Q^i = \frac{k_f^i}{\delta_f^i}(T_f^i - T_{fw}^i) \tag{25}$$

where k_f^i is the thermal conductivity of the water liquid film on the cooling plate. The heat transfer across the coolant wall can be calculated as:

$$Q^i = \frac{k_w^i}{\delta_c}(T_{fw}^i - T_{cw}^i) \tag{26}$$

where k_w^i is the thermal conductivity of the cooling plate. For the coolant channel (the wall bounding the coolant channel to the right shown in Figure 1 is assumed to be solid and adiabatic), the energy balance gives:

$$Q^i dx^i W = m_c^i (cp_{cb}^i T_{cb}^i - cp_{cb}^{i-1} T_{cb}^{i-1}) \tag{27}$$

where m_c and cp_{cb} are the mass flow rate and specific heat of the coolant.

Also, the heat transfer in the coolant channel can be calculated as:

$$Q^i = H_c^i (T_{cw}^i - T_{cb}^i) \tag{28}$$

where H_c^i is the convective heat transfer coefficient of the coolant channel.

To correct for changes in the fluid conditions as they flow through the AGMD module the correlation equations for the thermal properties presented in Table 1 were used.

Table 1: Correlation equations of seawater physical properties.

2.1.Solution procedure

The solution to the co-current and counter-current regimes begins by re-arranging equation (12) to take the following form:

$$\frac{J_v}{C} = P'_{hm} - P'_{ma} \tag{29}$$

From Equations (22) and (17):

$$J_v{}^i = M_v{}^i \bar{J}_v{}^i = \frac{cD_{AB}{}^i M_v}{\delta_a}(y_{ma}{}^i - y_f{}^i) = \frac{cD_{AB}{}^i M_v}{\delta_a}\left(\frac{P'_{ma}{}^i}{P} - \frac{P'_f{}^i}{P}\right) \tag{30}$$

Since $\rho = cM_v$ then the mass flux becomes:

$$J_v = \frac{cM_m D_{AB}{}^i M_v}{\delta_a P M_m}(P'_{ma}{}^i - P'_f{}^i) = \frac{\rho D_{AB}{}^i M_v}{\delta_a M_m P}(P'_{ma}{}^i - P'_f{}^i) \tag{31}$$

Using the ideal gas law we get:

$$J_v = \frac{D_{AB}{}^i M_v}{\delta_a R_u T_{avg}{}^i}(P'_{ma}{}^i - P'_f{}^i) = A(P'_{ma}{}^i - P'_f{}^i) \tag{32}$$

$$A^i = \frac{D_{AB}{}^i M_v}{\delta_a R\, T_{avg}{}^i} \tag{33}$$

From Equation (32), we obtain:

$$\frac{J_v{}^i}{A^i} = P'_{ma} - P'_f \tag{34}$$

Combining Equations (29) and (34) gives:

$$\left(\frac{1}{C^i} + \frac{1}{A^i}\right)J_v{}^i = P'_{hm}{}^i - P'_f{}^i$$
$$J_v{}^i = \left(\frac{1}{C^i} + \frac{1}{A^i}\right)^{-1}(P'_{hm}{}^i - P'_f{}^i) \tag{35}$$

where P'_{hm} and P'_f are the saturation pressures at the corresponding temperatures.

From Equations (5), (20), (23) we get:

$$\frac{Q^i}{H_h{}^i} = T_{hb}{}^i - T_{hm}{}^i$$
$$\frac{Q^i - J_v{}^i h_g{}^i}{k^i / \delta_m{}^i} = T_{hm}{}^i - T_{ma}{}^i \tag{36}$$
$$\frac{Q^i - J_v{}^i h_g{}^i}{k_{AB}{}^i / \delta_a{}^i} = T_{ma}{}^i - T_f{}^i$$

Combining the three equations above, we get:

$$\frac{Q^i}{H_h{}^i} + \frac{Q^i - J_v h_g{}^i}{k^i / \delta_m{}^i} + \frac{Q^i - J_v{}^i h_g{}^i}{k_{AB}{}^i / \delta_a{}^i} = T_{hb}{}^i - T_f{}^i \tag{37}$$

From equations (25), (26), (28):

$$\frac{Q^i}{k_f^{\;i}/\delta_f^{\;i}} = T_f^{\;i} - T_{fw}^{\;i}$$

$$\frac{Q^i}{k_w^{\;i}/\delta_c^{\;i}} = T_{fw}^{\;i} - T_{cw}^{\;i} \tag{38}$$

$$\frac{Q^i}{H_c^{\;i}} = T_{cw}^{\;i} - T_{cb}^{\;i}$$

Combining the three equations of (38) results in:

$$Q^i\left(\frac{1}{k_f^{\;i}/\delta_f^{\;i}} + \frac{1}{k_w^{\;i}/\delta_c^{\;i}} + \frac{1}{H_c^{\;i}}\right) = T_f^{\;i} - T_{cb}^{\;i} \tag{39}$$

For co-current flow, the calculation starts by estimating T_f^i where the mass flux (J_v^i) can be calculated from equation (35), the mass flux is then used in equations (24) and (37) to calculate the film thickness of the condensate (δ_f^i) and Q^i, respectively. At steady state, Q^i in equations (37) and (39) are equal. Therefore, equation (39) is used to re-calculate T_f^i. The above steps can be repeated until convergence. After the convergence of T_f^i, the feed flow rate and its bulk temperature and the temperature of the coolant of the next slice can be calculated from

$$m_h^{\;i+1} = m_h^{\;i} - J_v^{\;i} dx^i W \tag{40}$$

$$S^{i+1} = \frac{m_{hb}^{\;i} S^i}{m_{hb}^{\;i+1}} \tag{41}$$

$$T_{hb}^{\;i+1} = \frac{(Q^i dx^i W + m_h^{\;i} Cp_{hb}^{\;i} T_{hb}^{\;i})}{Cp_{hb}^{\;i} m_h^{\;i+1}} \tag{42}$$

$$T_{cb}^{\;i+1} = T_{cb}^{\;i} + \frac{Q^i dx^i W}{Cp_{cb}^{\;i} m_c^{\;i}} \tag{43}$$

In the above equations, *i+1* means the position of x_{i+1}. The above procedures can be performed from *x =0* to *x = L* (the length of the module). However, for counter-current flow, the solution is complicated by not knowing the exit temperature of the coolant fluid at x=0. Thus, the exit temperature of the coolant should be estimated first. Since the coolant exit temperature is always expected to be between the coolant inlet temperature and the inlet hot feed temperature, the average of these temperatures can be used as an initial estimate of the coolant exit temperature. The same co-current procedure is then used to calculate the inlet temperature of the coolant except that the equations 40, 42 and 43 are changed into the following equations:

$$m_h^{\;i+1} = m_h^{\;i} + J_v^{\;i} dx^i W \tag{44}$$

$$T_{hb}{}^{i+1} = \frac{(Q^i dx^i W + m_h{}^i Cp_{hb}{}^i T_{hb}{}^i)}{Cp_{hb}{}^i m_h{}^{i+1}} \tag{45}$$

$$T_{cb}{}^{i+1} = T_{cb}{}^i - \frac{Q^i dx^i W}{Cp_{cb}{}^i m_c{}^i} \tag{46}$$

The calculation is terminated when the estimation of the coolant exit temperature results in a difference between the calculated coolant inlet temperature and the coolant inlet temperature used as an input for the model calculation was below a pre-specified tolerance (0.001 ℃). Figures 3 and 4 show the algorithms used for the solution procedures in both flow regimes.

Figure 3: Calculation algorithm of the co-current flow model.

Figure 4: Calculation algorithm of the counter-current flow model.

3.   Materials and methods

3.1. Experimental setup and membranes

Two commercially available hydrophobic micro-porous polytetrafluoroethylene (PTFE) membranes with different mean (average) pore sizes (0.2 µm and 0.45 µm) provided by Sterlitech Corporation were tested in the AGMD process. The porosity and thickness of both membranes are 80 % and 100 µm each, respectively. Figure 5 shows the Scanning Electron Microscopy (SEM) of these membranes and its contact angle. These data were used in Eq. (18) to calculate the membrane mass transfer coefficient. A tortuosity of 1.5 for the pore structure was assumed.

Figure 5: Scanning electron microscopy (SEM) of the active layer (left), support layer (middle) and contact angle measurement of the commercial membranes.

Membrane sample of (5cm x 10cm) was tested in an AGMD flat sheet module made of polymethyl meth-acrylate (Figure 6b) locally designed and fabricated [36]. The channel height was 2 mm for both feed and permeates sides. In each channel a single sized filament spacer made of polypropylene was inserted. The spacer thickness was 0.8 mm with filaments diameter of 0.4 mm crossing each other with an angle of 90°. The membrane module was mounted vertically in a

bench scale set up. The permeate was collected from the bottom of the module in a flask placed on an electronic Mettler Toledo balance (ML3002E Precision Balance, with readability of 0.01 g) after it was condensed on a 0.25 mm thick stainless steel sheet. The air gap width was varied by using different thicknesses of polymethyl methacrylate frames inserted between the membrane and the condensation plate (3, 9 and 13 mm; however, it was technically very difficult to build a module with smaller air gap widths). The increase in the permeate weight was logged every 60 seconds via data acquisition software (Labview) to a computer hard drive. Deionized water and Red Sea water were used as feed solutions and filtered through a 5 µm filter to remove large suspended solids, while deionized water was used as coolant. Feed and coolant temperatures were monitored by in-line Pt100 sensors inserted at the entrance of the membrane module, and were used to control the heater and chiller temperatures via feedback control to the chiller and heater. A schematic diagram of the AGMD experimental unit is shown in Figure 6a.

Figure 6: a) Schematic of the AGMD experimental setup, b) Flat sheet AGMD module.

3.2. Experiment procedure

There are several features of the AGMD process that our mathematical model should be able to predict, such as the feed and coolant outlet temperatures, mass flux, and outlet feed salinity. However, not all of these features are important from a practical point of view and sometimes a feature can be very difficult to measure experimentally. The mass flux of the AGMD is considered as a very important feature should be measured with a high degree of accuracy especially in a bench scale study. Therefore, our validation procedure was based on comparing the predicted mass flux to the measured mass flux.

Reproducibility tests were initially conducted to determine the experimental error associated with flux measurements. A sensitivity analysis using the mathematical model was conducted to identify which operating parameters are likely to significantly affect the mass flux. A matrix of experimental runs was then planned (Table 2) to map the operating conditions for the AGMD process that would result in detectable variations in flux for the bench scale unit.

Table 2: Detailed conditions of the bench scale tests used in validating the model.

4. Result and discussion

4.1. Model validation at different operating parameters

The first set of experiments was conducted to test the reproducibility and to determine the experimental errors. The measured water vapor flux at different feed water temperatures was repeatable and the variation in flux was a maximum of ± 0.12 kg/m^2·hr (2%).

The mathematical model results were then validated against different experimental data. Figure 7 shows a comparison between the predicted mass fluxes and the measured water vapor fluxes for a range of deionized feed water temperatures (40°C – 80°C). The model predicted an exponential behavior of the AGMD flux as a function of feed water temperature. Such behavior is not only supported by our experimental data but also reported in published AGMD literature [14,17,37]. However, the validity of the mathematical model should not be judged based on predicting the trend of the process but also on how closely it predicts the absolute experimental data. Our current purpose of developing this model is to utilize it as a tool for further analyzing the AGMD process and for scale-up. Such a goal may require relaxed a criterion toward which we may judge the validity of our module. Nonetheless, the prediction of the model was within the range of the experimental error.

Figure 7: Simulated and measured water vapor fluxes at different deionized feed water temperatures (runs no. 11-15).

To validate the model further we replaced the deionized water (feed) with Red Sea water to see how the model predicts the water vapor flux for a seawater salinity of 4.2 wt%. The distillate conductivity was continuously measured to check for any pore wetting that may took place and the distillate conductivity was always below 20 μS. As shown in Figure 8, the predicted water vapor flux was also within the range of experimental error.

Figure 8: Predicted and measured water vapor fluxes at different seawater feed temperatures (runs 1-5).

The effect of air gap width was also investigated. As shown in Figure 9, the model predicted a decay in flux as the air gap increased. This result agrees with the results reported by Kimra et al. [18] and Jonsson et al. [20]. However, the model prediction for water vapor flux at different air gap widths was not as good as were the predictions for variations in feed temperature. Analysis of the results showed that the water vapor flux was very sensitive to the change of air gap width, especially when it is very small. A reduction in air gap width results in higher production capacity and higher errors. These errors are more significant when the air gap width is very small. Therefore, any small error in measuring the gap width (i.e., by 0.1 mm) will affect the water vapor flux significantly. The error of our measurements to the gap width was about $\pm$ 0.5 mm. Our investigation showed that this was due to the deformation of the parafilm tape used in sealing the module. Further experimental tests with a modified module are required in the future to better evaluate the model prediction at small air gap width.

Figure 9: Predicted and measured water vapor fluxes as a function of air gap width (runs no 16-21).

Finally, the model was validated against experimental data using different membrane pore sizes. The model prediction was good enough ($\pm10\%$), although it didn't predict well the data (15%) at feed temperature of 70 ^{0}C for the 0.45μm membrane (Figure 10). In this region the flux is increasing significantly as feed temperature is increased, so variations in the inlet temperature will have a larger effect on the measured flux compared to measurements at lower feed temperatures, and the error of 15% appears reasonable.

Figure 10: Predicted and measured water vapor fluxes using different membrane pore sizes (runs no 1-5 and 22-26).

4.2. AGMD process parameters analysis

The previous validation tests were reasonably sufficient to provide enough confidence in the developed mathematical model. Therefore, the model was utilized for analyzing the complex and interrelated AGMD process parameters that are considered essential for scaling-up the MD process. The complexity of scaling-up a process comes from combining technical and economic

judgments prior to making any decision. For example, the thermal efficiency, the temperature gradient across and along the membrane, the flow rate, the membrane surface area, and the flow regimes all have technical and economical dimensions. Some of these parameters are discussed in the next section. The discussion will be based on the input data presented in Table 3 to the mathematical model.

Table 3: The input parameters of the mathematical model used in analyzing AGMD process.

4.2.1.Effect of flow regime

The developed model can simulate both counter-current and co-current flow regimes for flat sheet AGMD modules. Figure 11 and 12 show the temperature profile of the hot feed water and the coolant temperatures inside the module. It might not be obvious which one would yield the higher water vapor flux. The counter-current regime is characterized by constant temperature difference along the module (this fact might not be true if the coolant flow rate is not equal to the feed flow rate) while the co-current regime starts with a large temperature difference across the membrane and decreases as the fluids move along the membrane. The effect of the flow regime type on the water vapor flux will be discussed further in the next section.

Figure 11: Simulating temperature profile along the membrane in counter-current flow regime.
Figure 12: Simulating temperature profile along the membrane in co-current flow regime.

4.2.2.Effect of membrane length

In a flat sheet module, whether a spiral wound or a plate and frame configuration, as the membrane length increases the water vapor flux decreases (Figure 13). This behavior can be explained by observing the change in the temperature difference across the membrane. As the membrane length increases, enough time is provided for the fluids to exchange mass and heat across the membrane. Therefore, the decrease in the hot feed water temperature and the increase in the coolant temperature result in a decrease in the temperature difference across the membrane (the driving force of mass transfer). Therefore, a gradual decrease in the flux takes place.

Figure 13: Simulating the effect of membrane length on water vapor flux.

It is also observed that the decrease in the flux is faster in the co-current regime than in the counter current one. The effect on the total permeate can be calculated by integrating the flux along the membrane length. We found that, for a membrane length of 15 meters, the total permeate in a co-current regime is less than that of the counter-current regime by about 5%. This difference is expected to decrease as the membrane length decreases. However, in co-current regime, heat recovery cannot be applied which makes the process thermally inefficient. Thus, in the remaining discussion of this section, we will consider only the counter-current flow regime.

The effect of flow rate on water vapor flux is strongly linked to the membrane length. For a fixed membrane length and equal feed and coolant flow rates, the driving force (temperature difference across the membrane) increases as the feed and coolant flow rates were increased together (Figure 14). At infinite flow rate, the maximum temperature difference across the membrane that can be achieved is the difference between feed and coolant inlet temperatures: in our case, $\Delta T_{max} = 60^{\mathbf{o}}C$. As the flow rates decrease, there is more time for the fluids to exchange heat inside the module, resulting in lowering the temperature difference across the membrane. Therefore, depending on the residence time of the fluid inside the module the driving force will change. If we assume that the cross sectional area of the fluid channel is constant along the module which is usually the case, then we can relate the effect of flow rate and membrane length (module length) to the residence time using the following equations:

$$Residence\ time = \frac{Module\ volume}{Flow\ rate} = \frac{Cross\ sectional\ area * Module\ length}{Velocity * Cross\ sectional\ area} \qquad (47)$$

From the equation above we observe that increasing the residence time of the module can be achieved by either reducing the fluids flow velocity or increasing the membrane length. However, in scaling-up the AGMD module we can only manipulate these two interlinked parameters when they are within the module pressure drop limit. The increase in module pressure drop caused by these parameters should not reach the liquid entry pressure (LEP) of the membrane used. Thus, the increase in flux shown in Figure 14 and the experimental results reported by Winter et al. [5] can be attributed mostly to the increase in the temperature difference across the membrane and, to some extent, to the decrease in the temperature polarization effect. Decoupling the effect of temperature polarization from the effect created by the change in residence time through changing the fluid flow rate is quite challenging and might not give accurate results. For instance, in order to maintain the same residence time while increasing the

fluid velocity, the module length should be increased according to Eq. (47). Such a change in module length will change the process parameters in other aspects that lead to invalid comparison.

Figure 14: Simulating the effect of the flow rate on the temperature difference across the membrane (feed and coolant flow rates are maintained the same).

It is worth mentioning here that the majority of the laboratory-scale tests reported in the literature are conducted with small membrane areas and at relatively high fluid velocity. These conditions are considered to be favorable for high flux, especially when the ΔT between inlet temperatures of the fluids used in the test are relatively large (ΔT=40-60 ^oC). The flux at these conditions will be large and far from the flux expected using large scale modules. For example, the 7-meter long membrane test conducted by Winter et al. [5] resulted in a ΔT of less than 10 ^0C even though the feed enters the module at 80^0C and the coolant at 25^0C. This small driving force resulted in a water vapor flux that was slightly higher than 1 kg/m^2.hr at feed flow rate of 200 L/hr. The performance of the membrane in an AGMD configuration is not expected to play a major role at lower ΔT conditions, since the water vapor flux at these conditions is low and within the range achievable by available commercial membranes. For instance, Figure 10 shows a slight increase in flux as the pore size increases from 0.2 μm to 0.45 μm at $\Delta T = 60$ ^oC across the membrane. Additionally the thermal efficiency of AGMD is high because of the insulating properties of the air gap, so changes in the thermal performance of membranes do not have a significant effect on the thermal efficiency of the MD process. But what is the optimal ΔT that an MD module should operate at? The answer to this question will be discussed in the next section where thermal efficiency and process economics are taken into consideration.

4.2.3.AGMD Process thermal efficiency

MD is a thermally driven process that utilizes phase change to achieve separation. Conceptually**,** the thermal process is not an efficient technique for separation because the large energy required to vaporize water is directed toward separating the major component (95% of water) in the mixture [38]. The same concept is also applied in reverse osmosis where water is being pushed across the membrane to separate it from the minor components (salts).

In addition, the streams that leave the phase change separation process carry with them a large quantity of heat and if this heat is not recovered (latent heat) the process becomes inefficient. These main streams that leave the process are the brine and distillate.

An energy balance of the process shows that the maximum heat recovery is achieved when the process brine and distillate temperatures approach the feed inlet temperature. This of course requires exchanging the heat of the produced water vapor with the process feed and extending the size of the separation unit to allow the brine to lose its heat through vaporization until its temperature approaches the feed inlet temperature. In practice, the energy taken away by the water vapor is recycled back to the process feed stream through a condenser to reduce the energy input required to raise the feed temperature to the phase change temperature. Moreover, the phase separation is conducted at a broad range of temperatures by extending the size of the unit to reduce the energy loss through brine discharge. Both of these techniques are applied in the conventional thermal desalination processes such as multi stage flash (MSF). However, the increase of the unit size is limited by an increase in the capital cost of the unit. For example, the size of a MSF unit is limited typically to 24 stages (with brine recirculation) and the brine temperature exiting the unit is about 10-15 ^{0}C higher than the process feed temperature [34,38]. This relatively high brine temperature is considered as the major heat loss in the MSF unit and must be compensated by an external heat source to maintain continuity of the separation process. AGMD is operated according to the same principle (Figure 15).

Figure 15: Typical design of AGMD.

In a once-through process like the AGMD shown in Figure 15, one can apply mass and energy balance calculations on the feed stream to get the maximum achievable water recovery. This recovery ratio is limited by the heated feed and the brine discharge temperatures according to the following equations:

Mass balance:

$$m_F - m_D - m_B = 0 \qquad (48)$$

where m_F, m_D and m_B are the mass flow rates of the feed, distillate and brine streams, respectively

Energy balance:

$$m_f C_p T_F - m_D h_g - m_B C_p T_B = 0 \qquad (49)$$

where T_F and T_B are the temperatures of the heated feed and brine discharge, respectively, h_g is the average latent heat of vapor, and C_p is the average specific heat of the feed.

From equation (48), we get:

$$m_F C_p T_F - m_D h_g - (m_F - m_D) C_p T_B = 0 \qquad (50)$$

Re-arranging the equation give:

$$\frac{m_D}{m_F} = \frac{(T_F - T_B)}{(\frac{h_g}{C_p} - T_B)} \qquad (51)$$

In a process that has a heated feed entering at 80 °C and a brine discharged at 30°C, the water recovery is only 8.5%.

The heat input to this process can be calculated using the following equation:

$$Heat\ input = m_F c_p (T_F - T_0) \qquad (52)$$

Where, T_o is the temperature of the feed after it leaves the heat recovery section. From equations (51) and (52) we can calculate the specific heat requirement of the thermal process as:

$$Specific\ heat\ requirement = \frac{Heat\ input}{m_D}$$

$$Specific\ heat\ requirement = \frac{m_F c_p (T_F - T_0)}{\frac{m_F (T_F - T_B)}{(\frac{h_g}{c_p} - T_B)}} \qquad (53)$$

After simplification,

$$Specific\ heat\ requirement = \frac{T_F - T_0}{T_F - T_B} (h_g - c_p T_B) \qquad (54)$$

$(T_F - T_0)$ represents the driving force across the AGMD membrane and $(T_F - T_B)$ represents the temperature drop along the AGMD module (feed side). We are going to refer to the former as ΔT_{cross} and the later as ΔT_{drop}. Therefore, AGMD efficiency increases as ΔT_{cross} decreases or

ΔT_{drop} increases. As discussed earlier, decreasing the driving force temperature (ΔT_{cross}) can be achieved by increasing the residence time of the fluid inside the module through either extending the module length or lowering the fluids flow rates. Increasing ΔT_{drop} can be mainly achieved by increasing the heated feed temperature or lowering the brine discharge temperature. Even though the AGMD process can be operated at high temperature similar to MSF using steam, we are going to assume that only low grade waste heat or solar energy is available. Therefore, we can fix the T_F to 80 ºC. In this way, our mathematical model can show how an increase in module length or reducing feed flow rate would reduce ΔT_{cross} which in turn reduces the specific heat requirement of the AGMD process (Figure 16).

Figure 16: Simulating the change in heat required and water vapor flux as a function of residence time.

From the cost point of view, the saving in thermal energy consumption does not come free and appears as an additional investment cost associated with increased membrane surface area. This brings us to the question of what is the optimal ΔT_{cross} that one should operate the AGMD module at. A preliminary assessment can be made by considering the operational cost of the heat input to the process and the capital cost of MD membrane. In undertaking this analysis the following assumptions have been made:

- Energy cost: $0.05 per kwh (typical energy cost in the Middle East)
- Membrane cost: 36 $/m^2 [39] (different membrane prices were reported in the literature ranging from 10 to 100 $/m^2 [40,41] and since this technology is not yet implemented at large scale it is very difficult to predict a more accurate price of the membrane. However, we chose the price in [39] because it falls in the range reported by Camacho et al. [40] for membrane processes.
- Membrane life time: 5 years (typical membrane life in water industry)

Using the above costing figures along with our modeling prediction results, the graph in Figure 17 shows an optimal point where the total energy consumption and membrane costs are at the minimum. This value is expected to shift to less ΔT_{cross} as the cost of the membrane becomes lower. As ΔT_{cross} increases the total cost becomes dominated by the energy cost.

Figure 17: Simulated simple cost analysis of AGMD membrane and its energy use cost.

While this cost analysis provides some insight into economical tradeoffs between increased thermal efficiency and capital cost, a more detailed life cycle analysis would provide a better understanding of the cost issues associated with implementation of AGMD.

5. Conclusions

A co-current and counter-current flow 1-D mathematical model for a flat sheet module was developed from the fundamental equations of mass and heat transfer. The model calculations were based on dividing the AGMD module into different longitudinal zones. Normal to these zones the module was sliced into small cells. The governing mass and energy equations were applied to these slices and solved by iterative procedures. The model was then validated against several experimental tests at different conditions such as different feed water temperatures, feed salinity, membrane pore sizes, and air gap widths. The model prediction error was within $\pm$ 10%. The model was utilized in analyzing some of the complex and interrelated AGMD process parameters that are considered essential for scaling-up the process. The analysis showed that fluid residence time inside AGMD module is very important for scaling-up the process since it has direct effect on process flux and its thermal efficiency. The flux decreases as the membrane length increases while it increases as flow rate increases. Furthermore, the total water vapor flux in a co-current regime is always less than that of the counter-current regime. Additionally, the thermal efficiency of the process increases as the membrane surface area increases which causes the AGMD process to operate at low temperature difference across the membrane, leading to lower water vapor flux.

Nomenclature

b Membrane thickness (m)

C Membrane mass transfer coefficient ($kg/m^2 \cdot hr \cdot Pa$)

c Molar concentration ($kmole/m^3$)

c_p Water specific heat (kJ/kg^oC)

c_{phb} Water specific heat at the bulk temperature of the hot feed channel (kJ/kg^oC)

d Membrane pore size (m)

D_{AB} Diffusion coefficient of water vapor in air (m²/s)

d_f Filament diameter (m)

d_h Hydraulic diameter in a spacer filled channel (m)

g acceleration due to gravity (m/s²)

H_c Water film heat transfer coefficient of the coolant channel (kJ/m²·hr°C)

H_h Water film heat transfer coefficient of the hot feed channel (kJ/m²·hr°C)

h_g Enthalpy of water vapor (kJ/kg)

h_s Spacer thickness (m)

i   Slice index

J_{mv} Water vapor flux by molecular diffusion (kg/m²·hr)

J_{kv} Knudsen mass flux of water vapor (kg/m²·hr)

J_v Water vapor flux (kg/m²·hr)

k   average membrane thermal conductivity (W/m°C)

k_{air} air thermal conductivity (W/m°C)

k_f falling film thermal conductivity (W/m°C)

k_m membrane polymer thermal conductivity (W/m°C)

k_l liquid water thermal conductivity (W/m°C)

k_w cooling plate thermal conductivity (W/m°C)

K_s Spacer factor

L Membrane module length (m)

m_c Mass flow rate of the coolant (kg/hr)

m_h Mass flow rate of the hot feed (kg/hr)

m_F Mass flow rate of the heated feed in once-through AGMD process (kg/hr)

m_B Mass flow rate of brine discharge in once-through AGMD process (kg/hr)

m_D Mass flow rate of the distillate in once-through AGMD process (kg/hr)

M_v Molecular weight of water vapor (Kg/kmole)

Nu   Nusselt's Number

P   Total pressure of AGMD module (Pa)

P'_f Water vapor partial pressure at the air gap and water falling film interface (Pa)

P'_{ma} Water vapor partial pressure at the air gap and membrane interface (Pa)

P'_{hm} Water vapor partial pressure at the membrane and hot feed interface (Pa)

P_v Water vapor partial pressure (Pa)

Pr   Prandtl's Number

Q   Heat flux (kJ/m^2·hr)

Q_c Heat flux in the cold feed channel (kJ/m^2·hr)

Q_h Heat flux in the hot feed channel (kJ/m^2·hr)

Re   Reynold's number

R   Universal gas constant

T_{avg} Average temperature inside the membrane (^{o}C)

T_B Temperature of the brine discharge in a once-through AGMD process (^{o}C)

T_{cb} Bulk temperature of the coolant (^{o}C)

T_{cw} Temperature of the cooling wall surface in the coolant channel (^{o}C)

T_f Temperature of the falling film at the interface between the film and the air (^{o}C)

T_F Temperature of the heated feed in a once-through AGMD process (^{o}C)

T_{fw} Film temperature in contact with the cooling wall (^{o}C)

T_{hb} Bulk temperature of the hot feed (^{o}C)

T_{hm} Temperature at the interface of hot feed and the membrane (^{o}C)

T_{ma} Temperature at the surface of the membrane facing the air channel (^{o}C)

T_o Temperature of the feed after it leaves the heat recovery section in a once-through AGMD process (^{o}C)

U_c Overall heat transfer coefficient of the coolant channel (kJ/m^{2}hr^{o}C)

U_h Overall heat transfer coefficient of the feed channel (kJ/m^2·hr·^{o}C)

V Average velocity of water (m/hr)

$V_{filament}$ Volume occupied by the filament (m^3)

V_{total} Total volume of the spacer (m^3)

W   width of the flat sheet module

x   Length of AGMD module (m)

y   Mole fraction of water vapor

y_f Mole fraction of water vapor at the interface of the falling film

y_{ma} Mole fraction of water vapor at the membrane-air gap interface

Greek symbols

δ_a	Width of the air gap (m)
δ_c	Thickness of the coolant wall (m)
δ_m	Thickness of the membrane (m)
δ_f	Thickness of the falling film (m)
ε	Membrane porosity
ε_s	Spacer porosity
θ	Angle between filaments (°)
ρ	Water density (kg/m^3)
ρ_{av}	Average liquid density (kg/m^3)
ρ_l	Liquid water density (kg/m^3)
τ	Membrane pores tortuosity
μ	Water dynamic viscosity (Pa·s)

References

[1]   H. Maab, L. Francis, A. Al-Saadi, C. Aubry, N. Ghaffour, G.L. Amy and S.P. Nunes, Synthesis and fabrication of hydrophobic polyazole membranes for seawater desalination, Journal of Membrane Science 423-424 (2012) 11-19.

[2]   Y.D. Kim, K. Thu, N. Ghaffour, K.C. Ng, A long-term performance investigation of solar-assisted hollow fiber DCMD desalination system, Journal of Membrane Science 427 (2013) 345-364.

[3]   E. Curcio, E. Drioli, Membrane distillation and related operations - A review, Separation and Purification Reviews 34 (2005) 35-86.

[4]   A.A. Hussain, J.M. Matar, R. Dores, C. Maltesh, S. Adham, Sustainable water production by membrane distillation using low grade waste heat, World Congress/Perth Convention and Exhibition Centre (PCEC), Perth, Western Australia September 4-9, 2011, Ref. IDAWC/PER11-094.

[5] D. Winter, J. Koschikowski, M. Wieghaus, Desalination using membrane distillation: Experimental studies on full scale spiral wound modules, Journal of Membrane Science 375 (2011) 104-112.

[6] A. Kullab, Desalination using membrane distillation: Experimental and numerical study, Doctoral Thesis 2011, Royal Institute of Technology, SE-100 44 Stockholm.

[7] J.H. Hanemaaijera, J.V. Medevoorta, A.E. Jansena, C. Dotremontb, E.V. Sonsbeekb, T. Yuanc, L. De Ryckb, Memstill membrane distillation – a future desalination technology, Desalination 199 (2006) 175–176.

[8] Z. Kui, W. Heinzl, F. Bollen, G. Lange, G. Van Gendt, A. Fane, Demonstrating solar-driven membrane distillation using Memsys vacuum-multi-effect-membrane-distillation, World Congress/Perth Convention and Exhibition Centre (PCEC), Perth, Western Australia September 4-9, 2011 Ref.: IDAWC/PER11-214.

[9] R.B. Saffarini, E.K. Summers, H.A. Arafat,Technical evaluation of stand-alone solar powered membrane distillation systems, Desalination 286 (2012) 332-341.

[10] N. Ghaffour, The challenge of capacity building strategies and perspectives for desalination for sustainable water use in MENA, Desalination & Water Treatment 5 (2009) 48-53.

[11] C. Bier, U. Plantikow, Solar-Powered Desalination by Membrane Distillation (MD), IDA World Congress on Desalination and Water Sciences, Abu Dhabi, November 18-24, 1995.

[12] A. Cipollina, M.G. Di Sparti, A. Tamburini, G. Micale, Development of a Membrane Distillation module for solar energy seawater desalination, Chemical Engineering Research and Design 90 (2012) 2101‑2121.

[13] H. Chang, C.L. Chang , C.D. Ho, C.C. Li, Wang, P.H., Experimental and simulation study of an air gap membrane distillation module with solar absorption function for desalination, Desalination and Water Treatment 25 (2011) 251-258.

[14] M.A. Izquierdo-Gil, M.C. Garcia-Payo, C. Fernandez-Pineda, Air gap membrane distillation of sucrose aqueous solutions, Journal of Membrane Science 155 (1999) 291-307.

[15] F.A. Banat, J. Simandl, Desalination by membrane distillation: A parametric study, Separation Science and Technology 33(1998) 201-226.

[16] G.L. Liu, C. Zhu, C.S. Cheung, C.W. Leung, Theoretical and experimental studies on air gap membrane distillation, Heat and Mass Transfer 34 (1998) 329-335.

[17] F.A. Banat, J. Simandl, Therotical and experimental study in membrane distillation, Desalination 95 (1994) 39-52.

[18] S. Kimura, S.I. Nakao, S.I. Shimatani, Transport phenomena in membrane distillation, Journal of Membrane Science 33 (1987) 285-298.

[19] C. Gostoli, G.C. Sarti, S. Matulli, Low-Temperature Distillation through Hydrophobic Membranes, Separation Science and Technology 22 (1987) 855-872.

[20] A.S. Jonsson, R. Wimmerstedt, A.C. Harrysson, Membrane distillation - a theoritical study of evaporation through microporous membranes, Desalination 56(1985) 237-249.

[21] A.M. Alklaibi, N. Lior, Transport analysis of air-gap membrane distillation, Journal of Membrane Science 255(2005) 239-253.

[22] R. Chouikh, S. Bouguecha, M. Dhahbi, Modelling of a modified air gap distillation membrane for the desalination of seawater, Desalination 181 (2005) 257-265.

[23] M.N. Chernyshov, G.W. Meindersma, A.B. de Haan, Modelling temperature and salt concentration distribution in membrane distillation feed channel, Desalination 157 (2003) 315-324.

[24] S. Bouguecha, R. Chouikh, M. Dhahbi, Numerical study of the coupled heat and mass transfer in membrane distillation, Desalination 152 (2003) 245-252.

[25] J. Zhang, J.-D. Li, S. Gray, M. Duke, N. Dow, Modelling for scale-up of membrane distillation processes, AWA Membranes and Desalination Specialty Conference III. 11-13 February, 2009, Sydney, NSW, paper 041.

[26] J. Zhang, J.-D. Li, S. Gray, Effect of applied pressure on PTFE membrane in DCMD, Journal of Membrane Science, 369 (2011) 514-525.

[27] J. Zhang, J.-D. Li, S. Gray, Researching and modeling the dependence of MD flux on membrane dimension for scale-up purpose, Desalination and Water Treatment 31 (2011) 144-150.

[28] J.H. Zhang, S. Gray, J.D. Li, Modelling heat and mass transfers in DCMD using compressible membranes, Journal of Membrane Science 387 (2012) 7-16.

[29] C.M. Guijt, G.W. Meindersma, T. Reith, A.B., De Haan, Air gap membrane distillation - 1. Modelling and mass transport properties for hollow fibre membranes, Separation and Purification Technology 43 (2005) 233-244.

[30] A.R. Dacosta, A.G. Fane, D.E. Wiley, Spacer Characterization and Pressure-Drop Modeling in Spacer-Filled Channels for Ultrafiltration, Journal of Membrane Science 87 (1994) 79-98.

[31] A.F. Mills, Mass transfer 2001: Prentice Hall.

[32] R.B. Bird, W.E. Stewart, E.N. Lightfoot, Transport phenomena2006: Wiley.

[33] H.D. Baehr, K. Stephan, Heat and mass transfer. 3rd rev. ed2011, Berlin ; New York: Springer. xxiv, 737 p.

[34] H.T. El-Dessouky, H.M. Ettouney, Fundamentals of Salt Water Desalination 2002: Elseivier.

[35] M.H. Sharqawy, J.H.L. V, S.M. Zubair, Thermophysical properties of seawater: A review of existing correlations and data, Desalination and Water Treatment 16 (2010) 354-380.

[36] L. Francis, H. Maab, A. AlSaadi, S. Nunes, N. Ghaffour, G.L. Amy, Fabrication of Electrospun Nanofibrous Membranes for Membrane Distillation Application, Desalination & Water Treatment 51 (2013) 1337–1343.

[37] M.C. Garcia-Payo, M.A. Izquierdo-Gil, C. Fernandez-Pineda, Air gap membrane distillation of aqueous alcohol solutions, Journal of Membrane Science, 169 (2000) 61-80.

[38] N. Ghaffour, T.M. Missimer, G.L. Amy, Technical review and evaluation of the economics of water desalination: Current and future challenges for better water supply sustainability, Desalination 309 (2013) 197-207.

[39] C. Liu, A. Martin, Applying membrane distillation in high purity water production for semiconductor industry, www.xzero.se, viewed July 2006.1.

[40] L.M. Camacho, L. Dumee, J. Zhang, J-D. Li, M. Duke, J. Gomez, S. Gray, Advances in Membrane Distillation for Water Desalination and Purification Applications, Water **5** (2013) 94-196.

[41] Y. Lu, J. Chen, Optimal Design of Multistage Membrane Distillation Systems for   Water Purification, Ind. Eng. Chem. Res. 50 (2011) 7345–7354.

Table 1: Correlation equations of seawater physical properties.

No	Property	Correlation	Reference
1	Water specific heat at constant pressure in kJ/kg.°C T = Temperature in °C Validity range: $10 \leq T < 180°C$ S = salinity in g/kg Validity range: $20 < S < 160$	$Cp = (A + BT + CT^2 + DT^3) \times 10^{-3}$ $A = 4206.8 - 6.6197\ S + 1.2288 \times 10^{-2}\ S^2$ $B = -1.1262 + 5.4178 \times 10^{-2}\ S - 2.2719 \times 10^{-4}\ S^2$ $C = 1.2026 \times 10^{-2} - 5.3566 \times 10^{-4} S + 1.8906 \times 10^{-6} S^2$ $D = 6.8777 \times 10^{-7} + 1.517 \times 10^{-6}\ S - 4.4268 \times 10^{-9}\ S^2$	[34]
2	Water dynamic viscosity in kg/m.s T=Temperature in °C Validity range: $20 \leq T < 180°C$ S = salinity in g/kg Validity range: $0 < S < 130$	$\mu = \mu_w \mu_R x 10^{-3}$ $\ln(\mu_w) = -3.79418 + \dfrac{604.129}{139.18 + T}$ $\mu_R = 1 + AS + BS^2$ $A = 1.474 x 10^{-3} + 1.5 x 10^{-6} T - 3.927 x 10^{-8} T^2$ $B = 1.0734 x 10^{-5} - 8.5 x 10^{-8} T + 2.23 x 10^{-10} T^2$	[34]
3	Water thermal conductivity in watt/m.°C T = Temperature in °C Validity range: $20 \leq T < 180°C$ S = Salinity in g/kg Validity range: $0 < S < 160$	$Log_{10}(k) = Log_{10}(240 + AS) + 0.434\,(2.3 - \dfrac{343.5 + BS}{T + 273.15})(1 - \dfrac{T + 273.15}{647.3 + CS})^{\frac{1}{3}}$ $A = 2 x 10^{-4}$ $B = 3.7 x 10^{-2}$ $C = 3 x 10^{-2}$	[34]
4	Enthalpy of saturated water vapor in kJ/kg T = Temperature in °C Validity range: 0.01-200 °C	$H = 2501.689845 + 1.806916015\ T + 5.087717 x 10^{-4}\ T^2 - 1.1221 x 10^{-5} T^3$	[34]
5	Latent heat of water evaporation in kJ/kg T = Temperature in °C Validity range: 5-200 °C	$\lambda = 2501.897149 - 2.407064037\ T + 1.192217 x 10^{-3}\ T^2 - 1.5863 x 10^{-5}\ T^3$	[34]
6	Pure water partial pressure in bar T = Temperature in K Validity range: $0 \leq T < 200°C$	$\ln\left(\dfrac{P_d}{P_{crit}}\right) = \dfrac{T_{crit}}{T} \sum_{i=1}^{8} b_i (1 - \dfrac{T}{T_{crit}})^{\frac{(i+1)}{2}}$ $P_{crit} = 220.93$, $T_{crit} = 647.25$ K $b_1 = -7.8889166$, $b_2 = 2.5514255$, $b_3 = -6.7161690$, $b_4 = 33.239495$, $b_5 = -105.38479$, $b_6 = 174.35319$, $b_7 = -148.39348$, $b_8 = 48.631602$	[5]
7	Correction for the seawater salinity effect on water vapor pressure S = salinity in g/kg Validity range: $0 < S < 130$	$\dfrac{P_v}{P_{v,sw}} = 1 + .57357(\dfrac{S}{1000 - S})$	[35]

Table 2: Detailed conditions of the bench scale tests used in validating the model.

Run No.	Variable parameter	Constant parameters
1-10	Temperature (40-80^{0}C) (reproducibility test)	Hot feed: Red Sea water Hot feed flow rate: 1.5 LPM Coolant fluid: Deionized water Coolant inlet temperature: 20^{0}C Coolant flow rate: 1.5 LPM Flow regime: Co-current Air gap width: 9 mm Pore size: 0.2 µm
11-15	Temperature (40-80^{0}C)	Hot feed: Deionized water Hot feed flow rate: 1.5 LPM Coolant fluid: Deionized water Coolant inlet temperature: 20^{0}C Coolant flow rate: 1.5 LPM Flow regime: Co-current Air gap width: 9 mm Pore size: 0.2 µm
16-21	Air gap width (5,9, and13mm)	Hot feed: Red Sea water Hot feed flow rate: 1.5 LPM Hot feed inlet temperature: 60,70^{0}C Coolant fluid: Deionized water Coolant inlet temperature: 20^{0}C Coolant flow rate: 1.5 LPM Flow regime: Co-current Pore size: 0.2 µm
22-26	Pore size (0.45µm)	Hot feed: Red Sea water Hot feed flow rate: 1.5 LPM Hot feed inlet temperature: 40-80^{0}C Coolant fluid: Deionized water Coolant inlet temperature: 20^{0}C Coolant flow rate: 1.5 LPM Flow regime: Co-current Air gap width: 9 mm

Table 3: The input parameters of the mathematical model used in analyzing AGMD process.

Fluids	Feed	Coolant	Membrane		Air gap width (mm)
Flow rate (LPM)	1-10	1-10	Width (m)	1	9
Temperature (^{0}C)	80	20	Length (m)	1-15	
Salinity (wt%)	4.2	0	Pore size (μm)	0.2	
Flow regime	Co-current & counter-current		Tortuosity	2	

Figure 1: A schematic diagram of AGMD longitudinal zones used in describing the model.
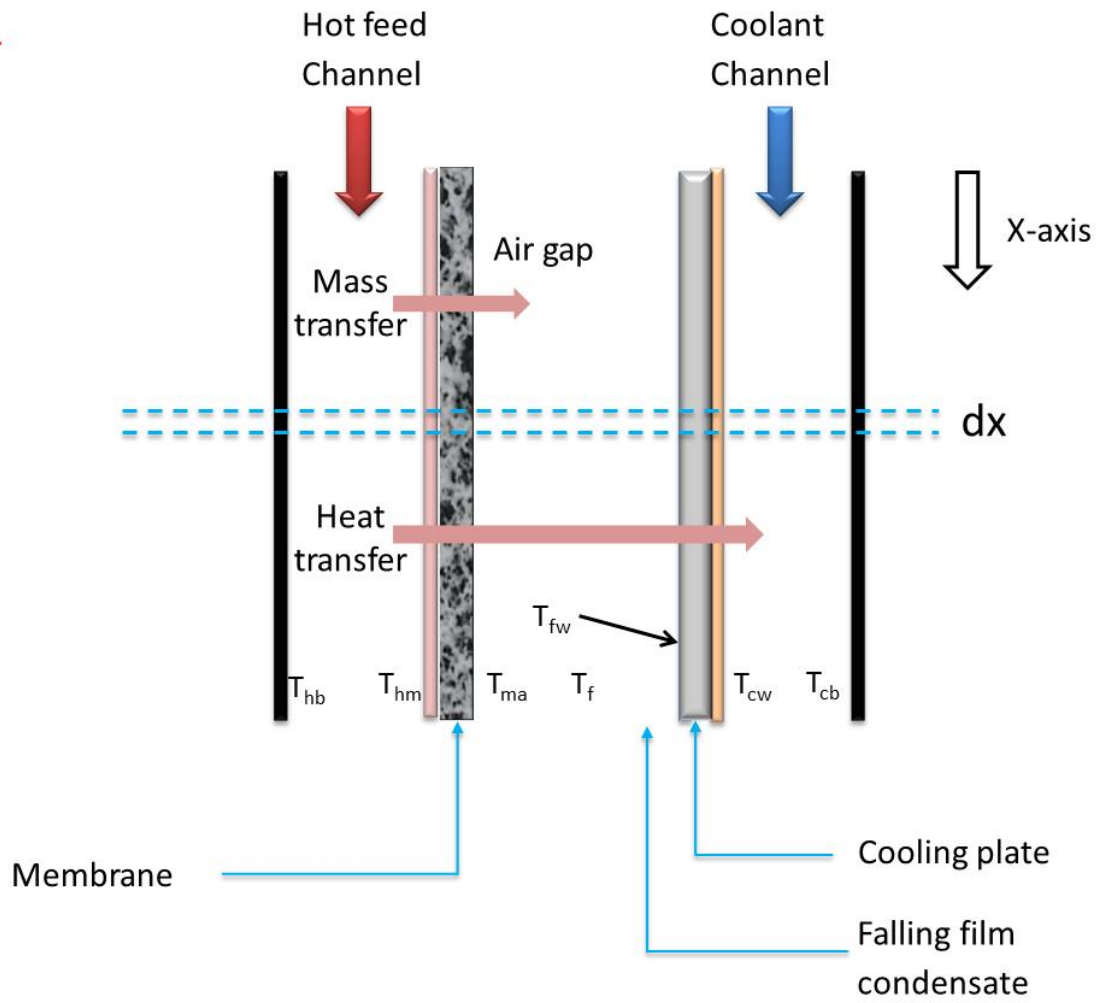
Slice i-1 $m^{i-1}c_p{}^{i-1}T^{i-1}$

$m_{i-1}c_{pi-1}T_{i-1}$

Slice i

$\Delta Q_h{}^i = (m_{hb}{}^i c_p{}^i T_{hb}{}^i - m_{hb}{}^{i-1} c_p{}^i T_{hb}{}^{i-1})/C$

$\Delta Q^i = (h_g J_v{}^i + U_h{}^i dx^i W(T_{hb}{}^i - T_f{}^i))/dx^i W$

$J_v = C \Delta P$

$U_c{}^i dx^i W(T_f{}^i - T_{cb}{}^i)$

$\Delta Q_c{}^i dx^i W = m_{cb} c_{pi}(T_{cb}{}^i - T_{cb}{}^{i-1})$

Slice i+1

$m_h{}^i c_p{}^i T_h{}^i$

$m_c{}^i c_p{}^i T_c{}^i$

Hot fluid channel

Hot fluid thin film

Membrane

Air gap

Cold fluid

Cold fluid thin film

Cooling plate

Film condensate
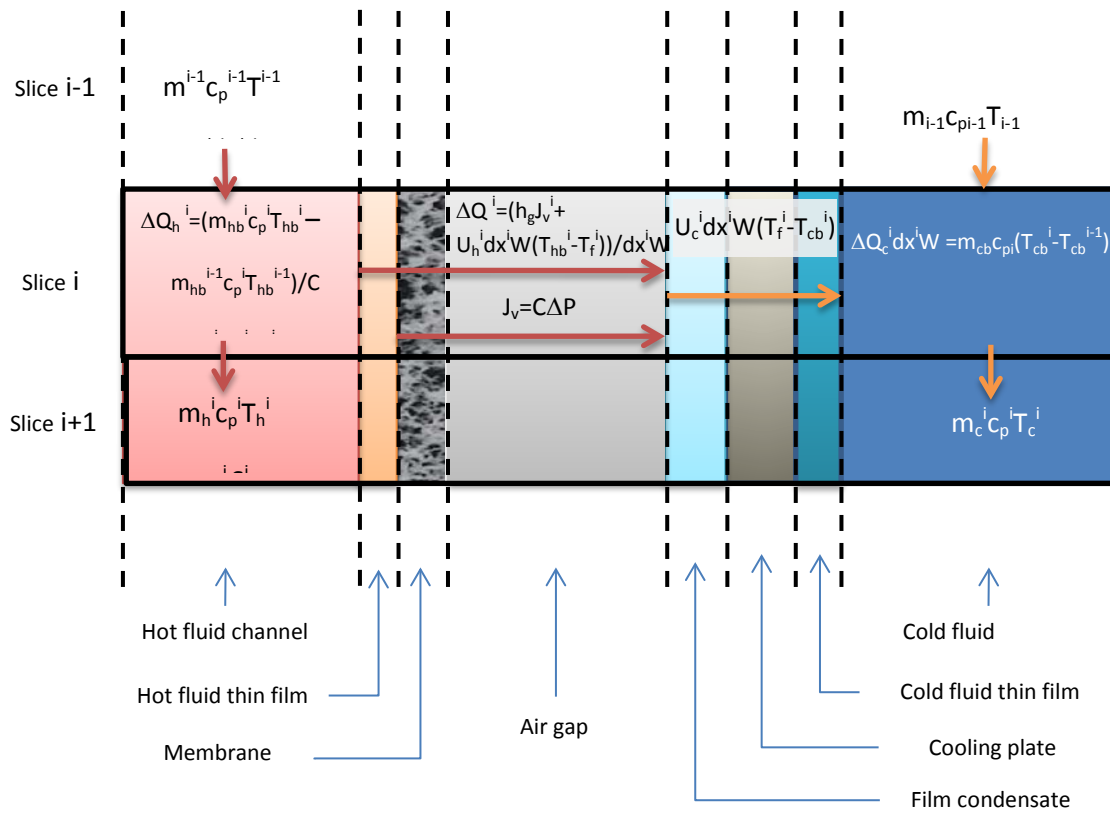
Figure 2: Magnification of two consecutive slices along an AGMD module.
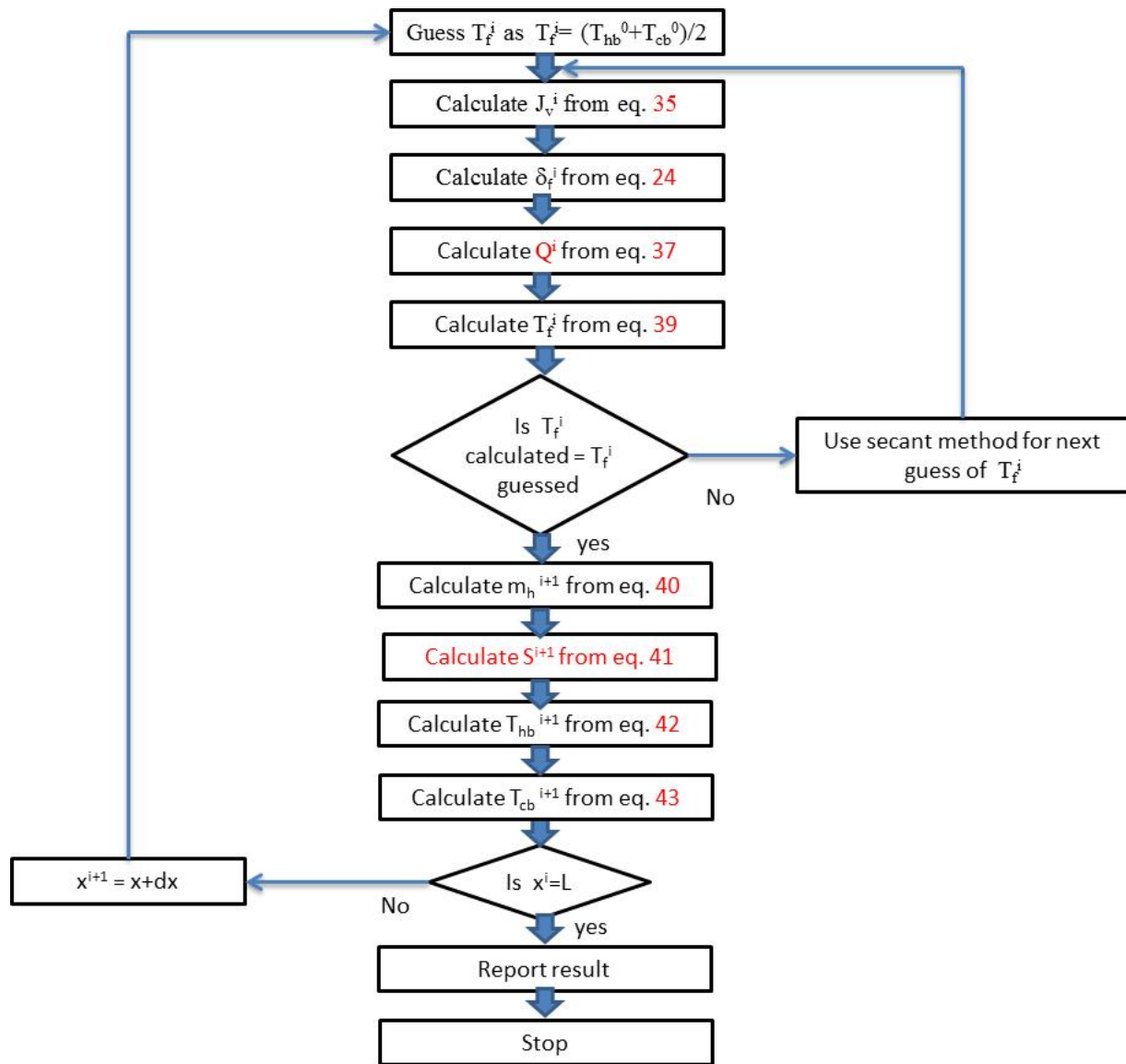
Figure 3: Calculation algorithm of the co-current flow model.
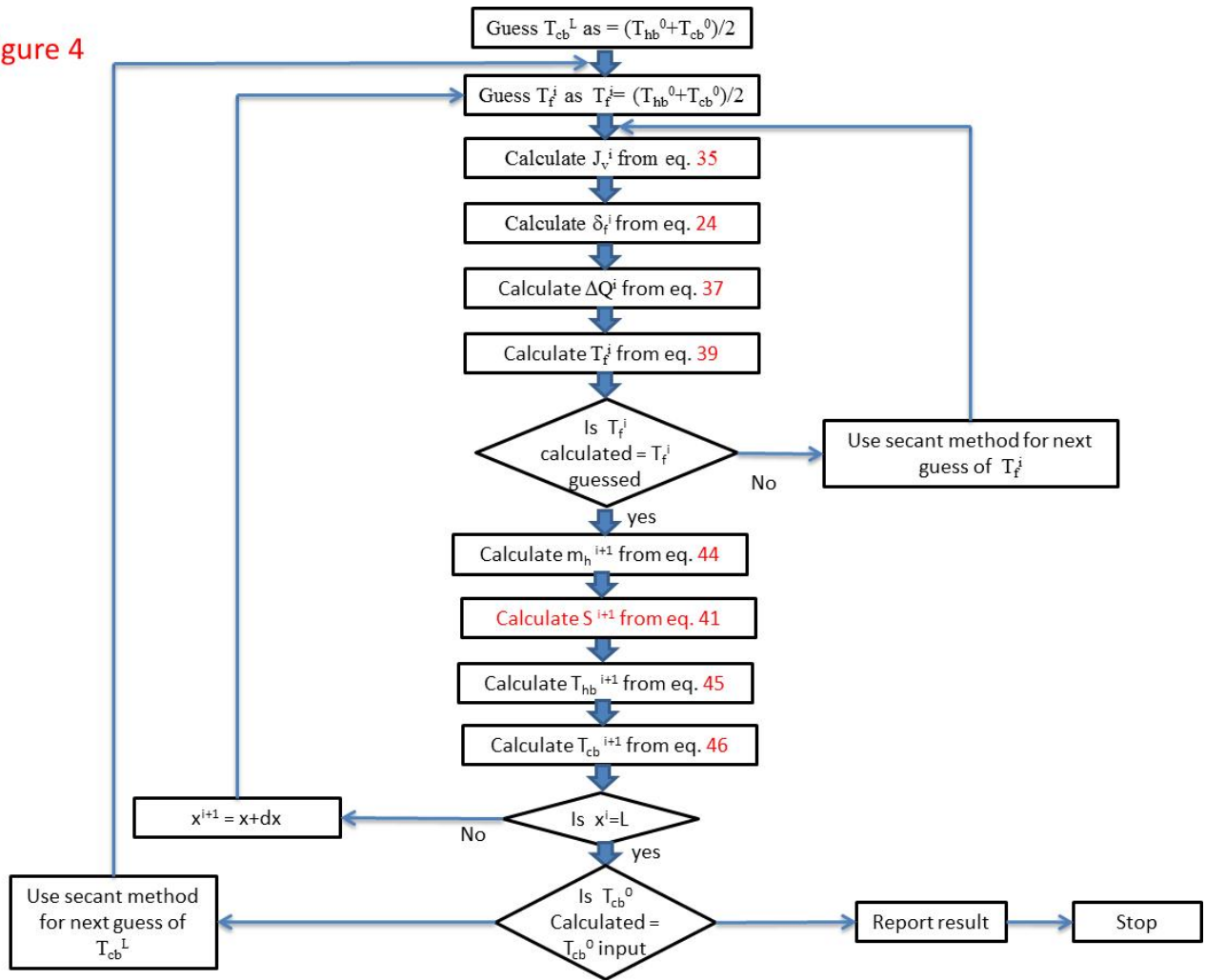
Figure 4

Figure 4: Calculation algorithm of the counter-current flow model.
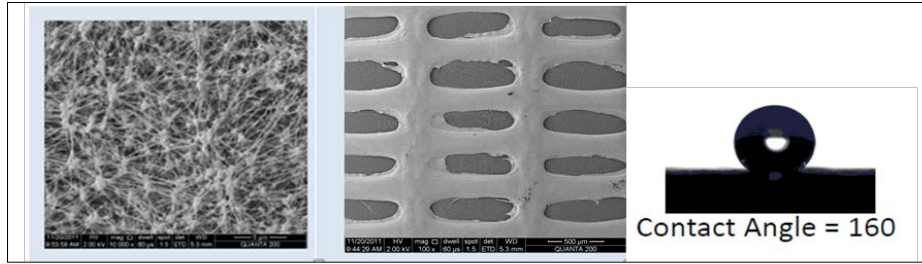
Figure 5: Scanning electron microscopy (SEM) of the active layer (left), support layer (middle) and contact angle measurement of the commercial membranes.
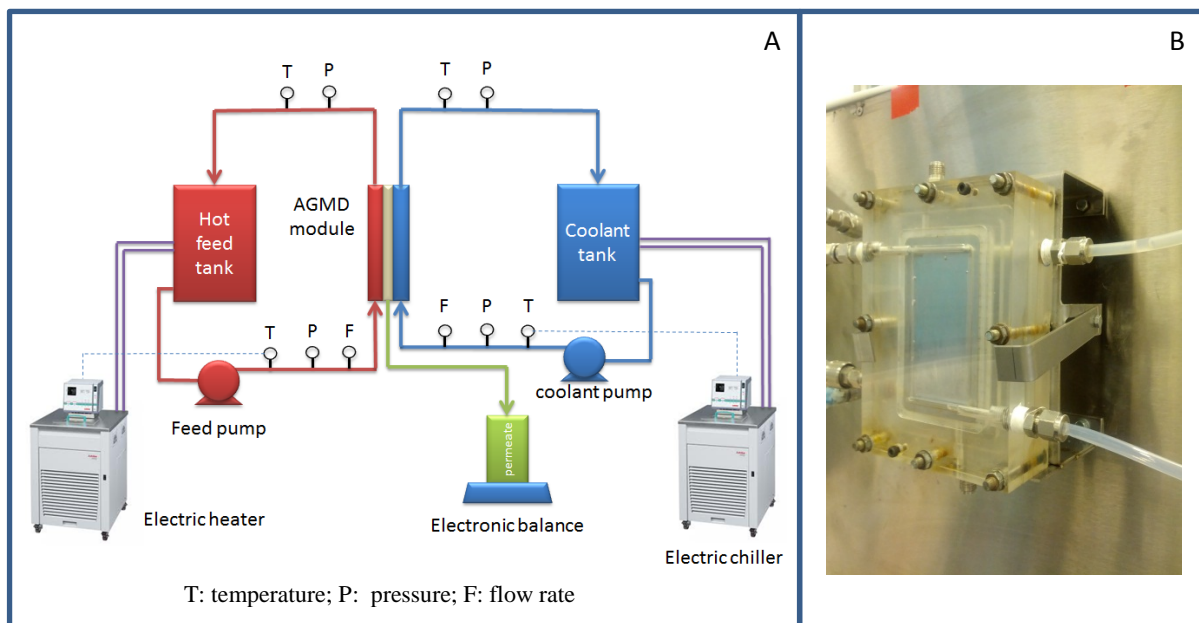
Figure 6: a) Schematic of the AGMD experimental setup, b) Flat sheet AGMD module.
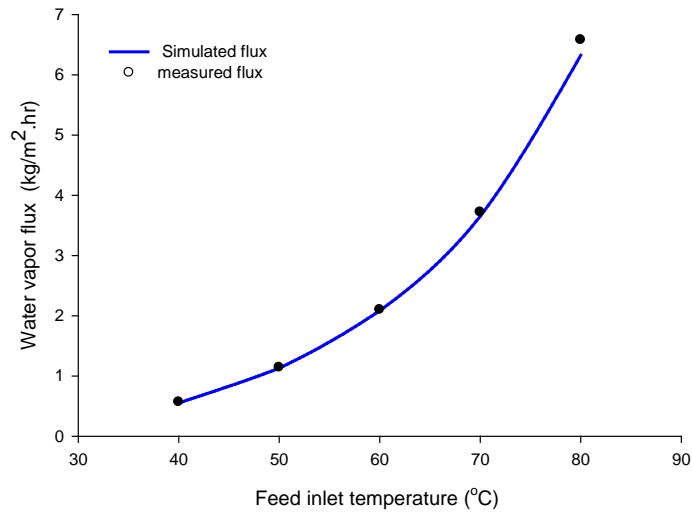
Figure 7: Simulated and measured water vapor fluxes at different deionized feed water

temperatures (runs no. 11-15).
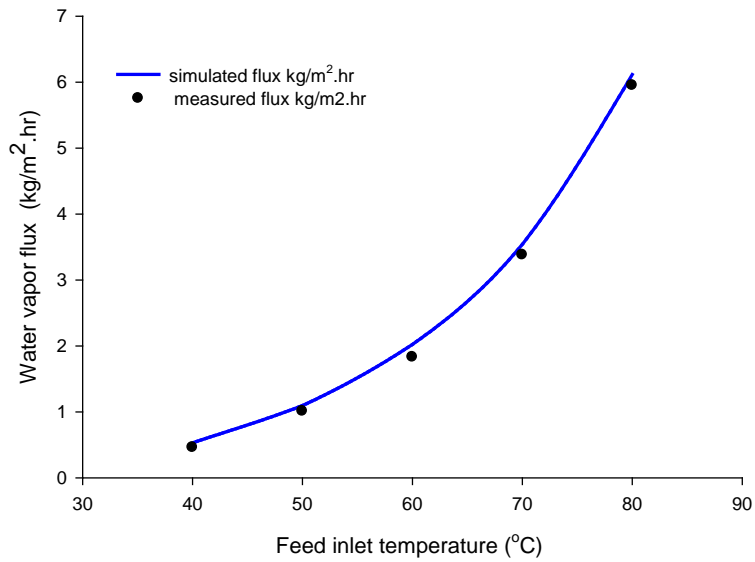
Figure 8: Predicted and measured water vapor fluxes at different feed seawater temperatures
(runs 1-5).
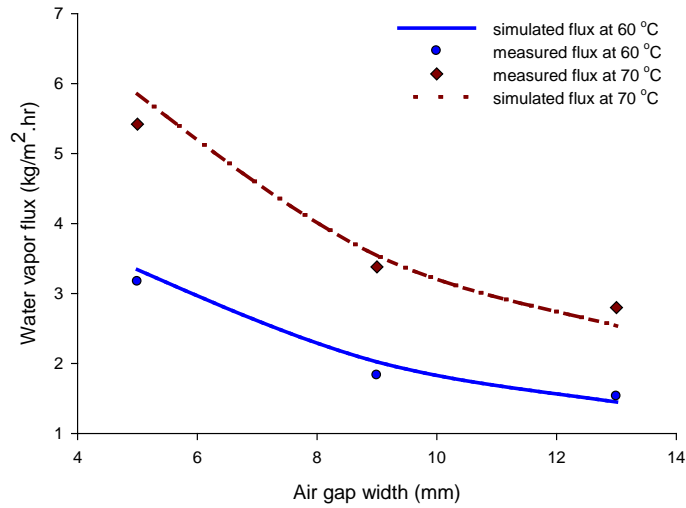
Figure 9: Predicted and measured water vapor fluxes as a function of air gap width (runs no 16-

21).
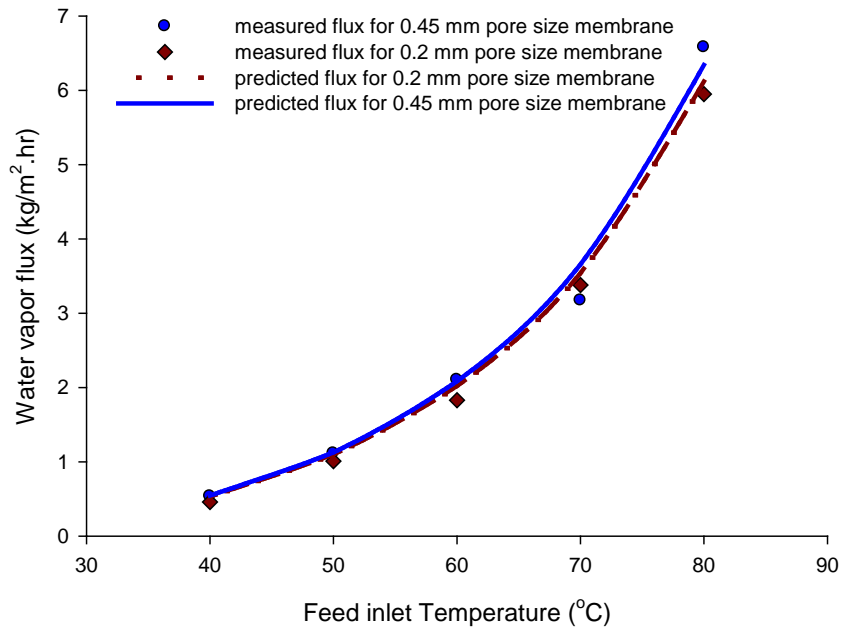
Figure 10: Predicted and measured water vapor fluxes using different membrane pore sizes (runs

no 1-5 and 22-27).
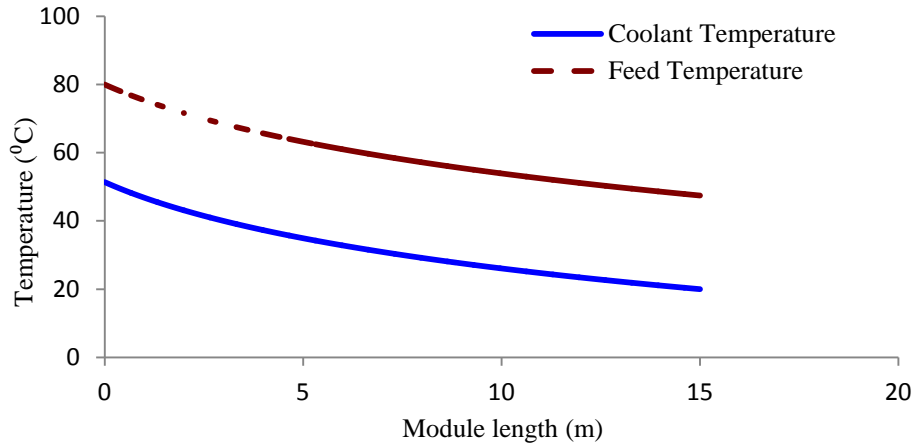
Figure 11: Simulating temperature profile along the membrane in counter-current flow regime.
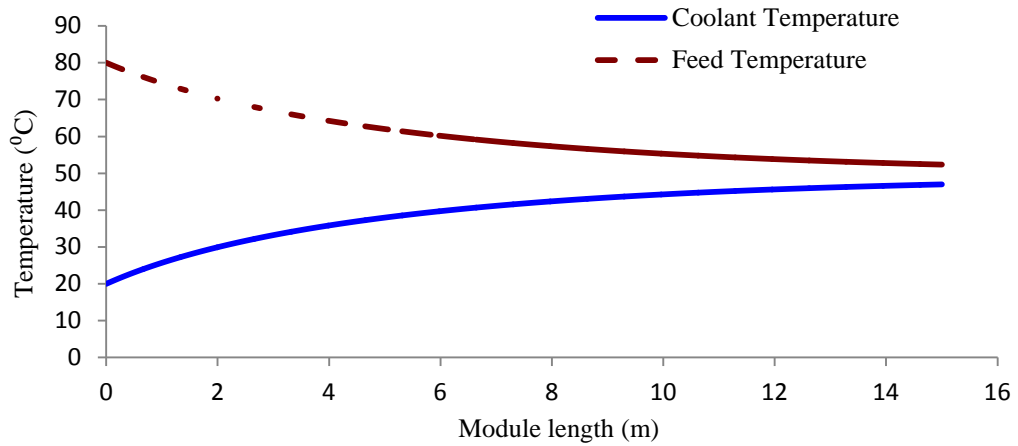
Figure 12: Simulating temperature profile along the membrane in co-current flow regime.
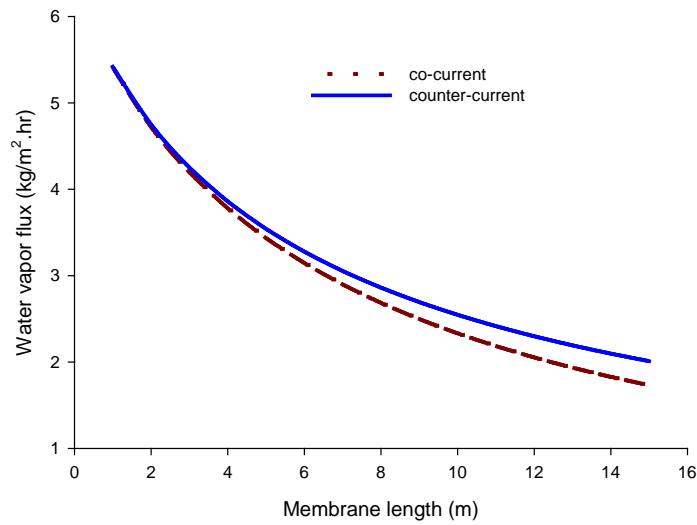
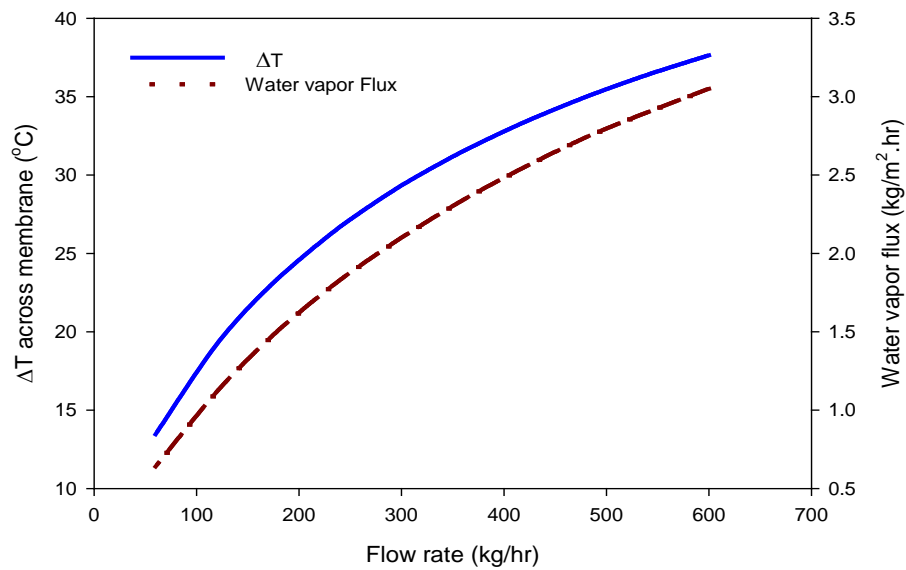Figure 13: Simulating the effect of membrane length on water vapor flux.

Figure 14: Simulating the effect of the flow rate on the temperature difference across the
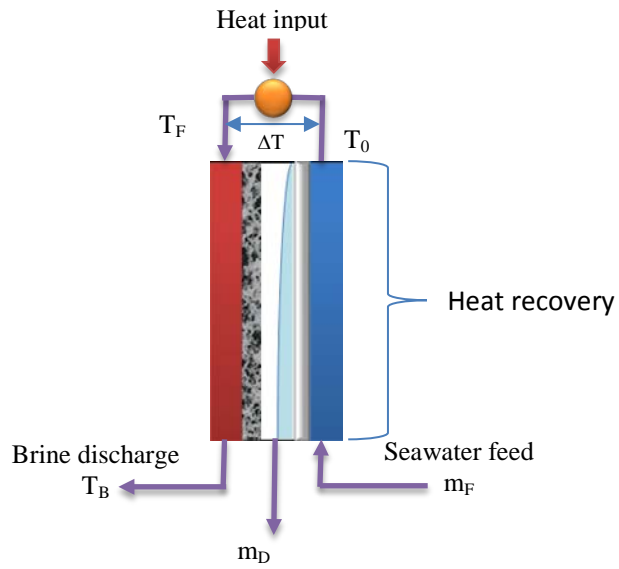membrane (feed and coolant flow rates are maintained the same).
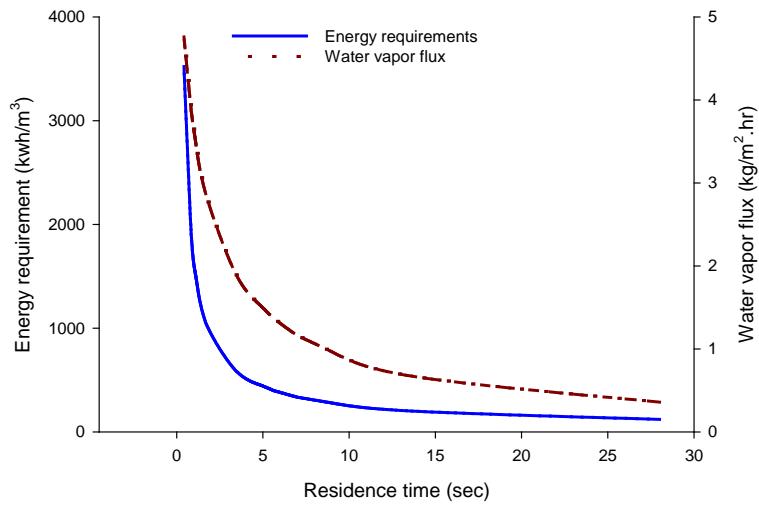
Figure 15: Typical design of AGMD.

Figure 16: Simulating the change in heat required and water vapor flux as a function of residence
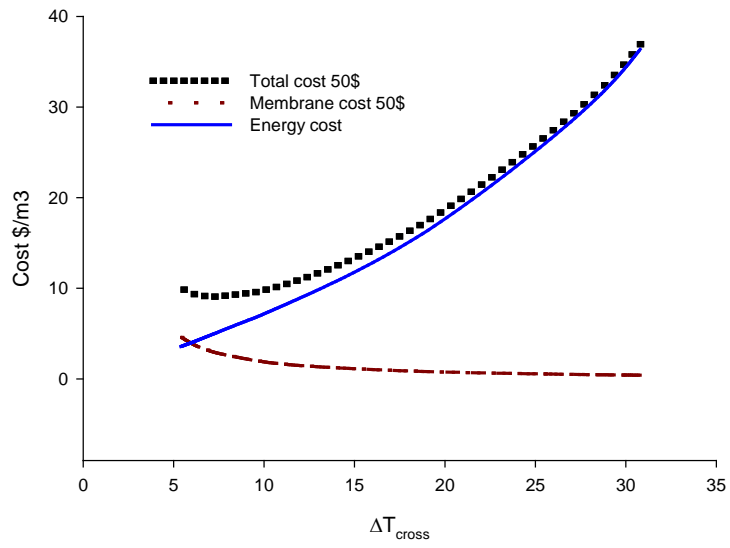
time.

Figure 17: Simulating simple cost analysis of AGMD membrane and its energy use cost.